

Evaluation of the Transmission Line Model for Couplant Layer Corrections in Pulse–Echo Measurements

Blake T. Sturtevant, Cristian Pantea, and Dipen N. Sinha

Abstract—An acoustic couplant layer plays an integral role in many ultrasonic nondestructive testing and material characterization applications. It is important to account for this layer for accurate time-delay measurements. In pulse–echo measurements, the couplant layer can be accounted for by modeling the frequency dependence of phase delay. In this paper, two such models are evaluated for robustness in determining an accurate phase velocity: a simple linear relationship and the acoustic transmission line with its associated nonlinear expression. For this evaluation, measurements of acoustic phase delay in an aluminum sample were made by the pulse–echo method using tone bursts of 1800 different carrier frequencies between 35 and 125 MHz. The transmission line model was fit to the measured data using an unconstrained nonlinear least squares fitting routine with two free parameters: the acoustic phase velocity in the sample and the couplant thickness. It was found that this nonlinear model was extremely sensitive to the initial parameter guesses and could not unambiguously determine both the couplant layer thickness and acoustic phase velocity. In contrast, the faster and simpler linear least squares fit to the delay data determines a unique phase velocity in agreement with resonant ultrasound spectroscopy, an independent measurement technique.

I. INTRODUCTION

IN ultrasonic pulse–echo (PE) experiments, one measures the delay between the time when an acoustic excitation (e.g., a tone burst) is launched by a piezoelectric transducer and the time when a response is received by the same transducer after having reflected off of a boundary or imperfection in the medium being studied [1], [2]. Highly accurate ultrasonic time-of-flight (TOF) measurements can play an important role in industrial process control, such as in thickness gauging and corrosion detection applications. A primary materials characterization application of PE that has been extensively used for over 60 years is for the determination of the fundamental properties, such as the elastic moduli, of matter [1]–[6]. When used for materials characterization, the measured time-of-flight is combined with measurements of the path length traversed by the acoustic wave to determine the acoustic phase velocity, v_p , along a given propagation direction. From determined phase velocities, one can extract material properties such as the elastic moduli and piezoelectric

constants. The PE technique has been widely used for the purpose of extracting material constants and, along with resonance techniques, is considered a standard for acoustic materials characterization [3]. The v_p s are related to the material density, ρ , and the elastic moduli, C , by $v_p^2 = C/\rho$ (where C can, in general, be a combination of many different elastic and piezoelectric constants). A relative error in phase velocity determination, $\delta v_p/v_p$, thus leads to a relative error in the elastic moduli of $\delta C/C = 2 \times \delta v_p/v_p$ if the density can be considered to be known to negligible uncertainty. Therefore, for accurate elastic constant determination, the importance of minimizing the relative error in v_p is clear.

The precision of a v_p extracted through PE measurements is typically $\sim 10^{-3}$ for samples of a few millimeters in size and is usually limited by measurement precision of the physical length of the sample, assuming that the TOF can be measured to at least an order of magnitude better in precision [4]. If the physical dimensions of the sample can be measured without bias, the accuracy of the determined phase velocity is limited entirely by the accuracy with which one can determine the TOF in the sample. In this work, a method for determining TOF to one part in ten thousand is presented. The present work focuses on the effectiveness of the 1-D scalar transmission line model commonly used to correct for the acoustic couplant layer that is used to enable energy transfer between a transducer or buffer rod and the sample in PE TOF measurements. A typical PE setup including the piezoelectric transducer, a buffer rod, the couplant, and the sample is shown schematically in Fig. 1. The couplant, exaggerated in thickness for clarity in the figure, introduces a phase shift to acoustic waves that are reflected from the buffer rod/couplant/sample interface (i.e., the ray labeled B in Fig. 1) and also those that are transmitted through this interface (i.e., the ray labeled C in Fig. 1). The phase shifts acquired by the acoustic waves upon reflection from and transmission through interfaces combine to lead to a difference between measured time delay (the delay between the arrival of echoes B and C in Fig. 1) and the actual transit time in the sample at any given frequency, f [4], [7]–[11]:

$$\tau_m = \tau_s + \varphi_{\text{net}}/2\pi f, \quad (1)$$

where τ_m is the measured TOF and τ_s is the desired TOF in the sample. φ_{net} describes the total phase difference between the two echoes being considered that does not result from the transit of the acoustic wave through the

Manuscript received July 25, 2012; accepted February 26, 2013. This work was supported by the U.S. Department of Energy (DOE) under award number AID 18832.

The authors are with Materials Physics and Applications, Los Alamos National Laboratory, Los Alamos, NM (e-mail: bsturtev@lanl.gov).

DOI <http://dx.doi.org/10.1109/TUFFC.2013.2651>

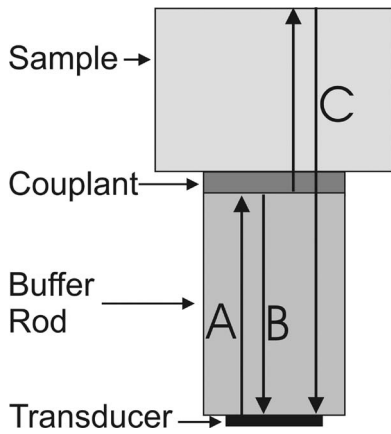


Fig. 1. A schematic of a typical pulse-echo transducer, buffer rod, couplant, and sample assembly. The incident acoustic wave and two possible reflections are depicted with arrows. The piezoelectric transducer converts the electrical signal into an input acoustic stress wave (labeled A) that is partially reflected (labeled B) from the buffer rod/couplant/sample interface, and partly transmitted (labeled C) into the sample.

sample. That is, φ_{net} is a result of the reflection from and transmission through the various interfaces in Fig. 1 by the acoustic wave. The need to account for this phase shift in determining the correct TOF in the sample has been recognized for many years [9] and has been addressed by several authors [4], [7]–[11]. It is interesting to note that the effects of the couplant can be avoided altogether through use of an immersion TOF technique such as is described in [12]. However, fluids do not support shear wave propagation and this limits immersion techniques to determination of longitudinal elastic moduli. The technique described in this work can be used for the determination of both longitudinal and shear elastic moduli provided that a shear-transmitting couplant (cyanoacrylate is a common choice) is used.

A common method of correcting for the acoustic couplant layer involves treating the buffer rod–couplant–sample system as a 1-D three-section transmission line, as is shown schematically in Fig. 2. In Fig. 2, an acoustic wave propagates in the $+x$ direction from the buffer rod, medium (1), toward the sample, medium (3). Medium (2) represents the couplant of thickness l_c . The A_j and B_j are the amplitudes of the various displacement waves, the k_j are the wave numbers of the waves in the various media, and $\omega = 2\pi f$ is the angular frequency of the wave. The complex amplitudes of the associated strain waves, A^{strain} , are found by taking the gradient of the displacement waves: $A^{\text{strain}} = A^{\text{displacement}} \times ik_j$ in the plane wave approximation. The amplitudes of the stress waves are that of the strain wave multiplied by the relevant stiffness, C , for the acoustic mode: $A^{\text{stress}} = A^{\text{strain}} \times C$. Using these relations and the imposition of continuity of normal displacement and strain at each of the two boundaries, one can derive the reflection and transmission coefficients of the various stress waves received at the transducer [10].

As discussed in Section III, (1) can be fit to experimentally measured PE delay data using the reflection and

transmission coefficients derived through this transmission line model to determine the acoustic phase velocity in the sample along with the couplant thickness. Because the reflection and transmission coefficients contain several trigonometric functions, fitting the model to the data requires the use of nonlinear least squares (NLLS) minimization routines, which are known to be sensitive to the initial guesses provided by the user [13]. It has been tacitly assumed in the literature that the accuracy of PE TOF determinations is improved by using the nonlinear transmission line model instead of simply fitting a linear model to (1) (i.e., to assume φ_{net} is constant at all frequencies). Earlier works have focused on fitting the transmission line model to data collected over a relatively low and narrow frequency range where φ_{net} is largely linear. However, the strongest nonlinearities in φ_{net} are present in the frequency ranges corresponding to acoustic resonances in the couplant layer. Because the thickness of the couplant layer is typically on the order of tens of micrometers or less, observation of these strong nonlinearities necessitates measuring delays at very high frequencies. The present work extends the bandwidth of PE measurements to include the strong nonlinearities in φ_{net} . Additionally, we present a thorough analysis of the effectiveness and sensitivity of NLLS minimizations when used to interpret acoustic pulse-echo delay data.

Section II describes the experimental setup and data collection procedure used. Section III briefly presents the scalar transmission line model and explains the signal processing and nonlinear searches used in this work. Section IV gives an analysis of the data collected in this work and Section V concludes the paper.

II. EXPERIMENTAL APPROACH

The experimental setup for the PE measurements is shown schematically in Fig. 3 and consists of a personal computer, an arbitrary function generator (AFG3102, Tektronix Inc., Beaverton, OR), a digital oscilloscope (DPO4034, Tektronix Inc.), and the transducer/buffer rod/sample assembly. The entire experimental setup re-

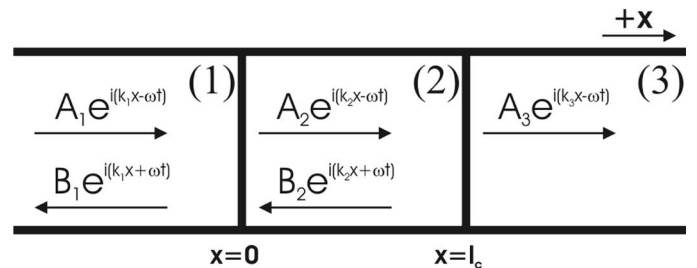


Fig. 2. The 1-D transmission line model that is commonly used to treat the couplant correction in pulse-echo time-of-flight measurements. A displacement wave with amplitude A_1 is shown here traveling in the $+x$ direction in the buffer rod (medium 1). The wave is partially reflected with amplitude B_1 and partially transmitted into the coupling layer (medium 2) and eventually into the sample (medium 3).

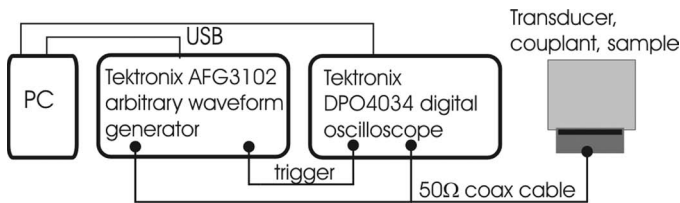


Fig. 3. A schematic of the experimental equipment setup used in this work. An arbitrary waveform generator creates a tone burst with a user-defined carrier frequency and modulation envelope which is converted into an acoustic stress wave by the piezoelectric transducer. All signals are recorded through a digital oscilloscope and stored on a PC which is also used for communicating with the instruments.

sides in a laboratory with an ambient temperature that is stabilized to within $\pm 1^\circ\text{C}$. The computer was used for communications with the function generator and oscilloscope and also to store the waveforms recorded from the oscilloscope. The DPO4034 oscilloscope has a maximum sample rate of 2.5 Gsample/s yielding a time resolution of ± 0.2 ns. The transducer used in this work had a center frequency of 125 MHz and came commercially packaged with a built-in fused silica buffer rod that provided a 2.5 μs delay (Olympus NDT Inc., Waltham, MA). The sample used was a right circular aluminum cylinder machined from stock Al available in our machine shop. The sample dimensions were 5.060 mm in height and approximately 12 mm in diameter. The diameter of the sample was chosen to be larger than the ~ 8.5 mm diameter of the buffer rod to minimize edge guiding effects, but had to remain smaller than 12.7 mm, a constraint imposed by the polishing equipment. The transmission line model, shown schematically in Fig. 2, assumes that the faces of the buffer rod and sample are flat and parallel. To ensure flatness, the two end faces of the cylindrical sample were ground and polished with successively finer diamond polishing compounds (Allied High Tech Products Inc., Compton, CA) down to a final grit size of 1 μm .

To efficiently transfer acoustic energy between the buffer rod and sample, the faces of these two parts must be nearly perfectly parallel. To ensure parallelism in these experiments, a careful alignment procedure was undertaken before measurements began. The setup for sample alignment is shown in Fig. 4. The transducer/buffer rod assembly was held stationary using a lab stand and clamp system. The sample was held in a separate clamp with two-axis tilt capabilities so that the face of the sample could be adjusted to be as parallel as possible to the face of the buffer rod. The up/down motion of the sample was coarsely controlled using the z -axis of an X-Y-Z linear positioning stage (NLS4-2-16-1, Newmark Systems Inc., Rancho Santa Margarita, CA) and finely controlled using a manual micrometer. To align the transducer and sample, a drop of water was deposited on the face of the buffer rod and the sample was lowered until it was in close contact with the buffer rod. A 0.5 - μs tone burst with a carrier frequency of 80 MHz was applied to the transducer. This signal, along with the echoes from the back faces of the buffer

rod and the sample, was displayed on the oscilloscope. The two tilt axes of the sample holder were adjusted until the amplitude of the sample back wall echo (ray C in Fig. 1) was maximized. When the sample and transducer faces were as parallel as achievable, the sample was lifted off of the transducer and the water was rinsed off both faces with isopropyl alcohol and blown dry. The sample was then brought just barely into contact with the transducer and the zero point on the micrometer was recorded. The sample was then lifted up and a small amount of Ultragel II ultrasonic couplant (Sonotech Inc., Glenview, IL) was applied to the transducer. Finally, the sample was lowered onto the transducer/couplant to the desired target thickness (~ 20 μm for the data presented in Section IV) using the micrometer. Through this alignment procedure, the parallelism of the sample and the buffer rod is estimated to be better than $\pm 0.2^\circ$. Such deviations from parallelism introduce an uncertainty in the round-trip path length of the acoustic wave on the order of 10 ppm, well beyond the precision that this dimension can be measured.

In the experiments reported here, a tone burst of 0.5 μs duration was used. The carrier frequency of the tone burst was modulated using a Tukey envelope [14] with an α value of 0.4. Alpha is a non-dimensional number between 0 and 1 and measures how sharply the modulated signal increases. An α of zero corresponds to a rectangular modulation window, whereas an α of unity value corresponds

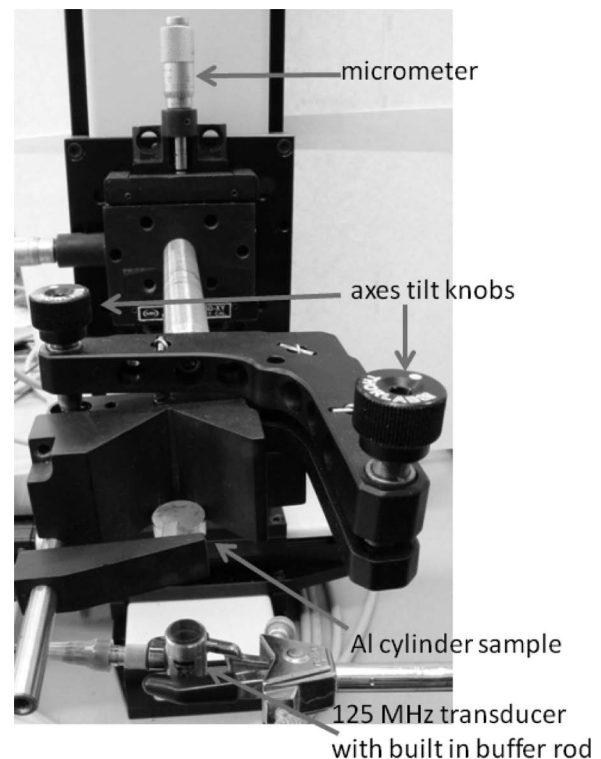


Fig. 4. The setup for aligning the sample and buffer rod faces. The transducer is held stationary using a lab stand and clamp; the sample is mounted in a clamp with two-axis tilt capabilities to adjust the plane of the sample until it is as parallel as possible to the plane of the buffer rod. Up-down motion is coarsely controlled using a linear translation stage and finely controlled with a micrometer, as described in the text.

to a half-period sine wave modulation window. The Tukey envelope was used to avoid sharp edges in the modulation which excite high-frequency transients in the transducer. Data were collected at frequencies between 35 and 125 MHz in 50 kHz steps for a total of 1800 data points. The center frequency of the transducer was used as the upper frequency bound of the measurements to avoid exciting the transducer's resonant frequency in addition to the drive frequency, which has been shown to lead to errors in TOF determination [10]. For each value of carrier frequency, a waveform that included the reflection from the buffer rod (ray B in Fig. 1) and the first reflection from the back of the sample (ray C in Fig. 1) was recorded. The data acquisition process for 1800 frequencies lasted six and one half hours.

The longitudinal sound speed and density of the couplant, two parameters that must be known when using the transmission line model, were determined by independent measurements. The sound speed was determined to be 1683 ± 4 m/s using swept frequency acoustic interferometry [15] between 1.0 and 4.0 MHz in a right circular cylindrical lead zirconate titanate (PZT) cavity. The density of the couplant was found to be 1040 ± 30 kg/m³ by massing a known volume of couplant. Both measurements were carried out at a laboratory ambient temperature of 22°C. The measured values were in agreement with those reported on the couplant manufacturer's product data sheet: velocity = 1650 ± 50 m/s and density = 1090 ± 65 kg/m³. Finally, resonant ultrasound spectroscopy (RUS) [16], an independent experimental method which does not utilize an acoustic couplant, was used to provide a set of elastic moduli against which to compare the PE results. In RUS, many resonant modes of a sample are measured and are used to determine the entire elasticity tensor, C , from measurement of a single sample. Publicly available code for analyzing RUS spectra are limited to regularly shaped samples of relatively high symmetry materials and do not include other material properties such as piezoelectricity.

III. THEORETICAL APPROACH

To determine the time delay between the reflections from the buffer rod and sample, the first two echoes in each waveform [labeled 1st buffer rod reflection and 1st sample reflection in Fig. 5(a)] were cross-correlated to give a cross-correlation function [17] such as the one shown in Fig. 5(b) (zoomed in around the maximum to show the details of the function). By summing random noise contributions, the cross-correlation procedure dramatically increases the SNR of the measurement. Calculated here as the peak-to-peak amplitude of the signal divided by that of the noise, the SNR was on the order of 100 after the cross-correlation procedure compared with the raw waveform SNR which was in the range of 5 to 10, depending on the carrier frequency being considered. For each frequency at which data were collected, the lag corresponding to the maximum of the cross-correlation function [solid black

circle in Fig. 5(b)] as well as the lags corresponding to the local maxima on either side of the maximum [open circles in Fig. 5(b)] were recorded. The cross-correlation function has the same periodicity as the input and reflected tone bursts and so the other local maxima are $\pm 2n\pi$ out of phase with the absolute maximum of the correlation function, where n is an integer. Following the approach used in [10], the time lag corresponding to the absolute maximum in the cross-correlation function for each frequency is plotted versus $1/f$; they are denoted with heavy black data points in Fig. 6. The time delay of the maxima on either side of the absolute maximum are also plotted and are shown as smaller gray points in Fig. 6. Such a plot is very useful for visualizing the $1/f$ dependence of the delay data. It is important to note from the figure that the absolute maximum in the cross-correlation does not always correspond to the delay which lies along the trace with the shallowest slope. This is a critical observation that emphasizes the importance of taking into account the additional local maxima on both sides of the absolute maximum in the cross-correlation result. Data can be easily rearranged such that the trace with the shallowest slope corresponds to $\varphi_{\text{net}}/2\pi f$. Because the delays of echoes measured at many different frequencies are considered in Fig. 6, the data appear to be continuous functions of $1/f$ rather than the discrete points of which they are actually composed. Each trace above and below this trace depends on $1/f$ as $(\varphi_{\text{net}} + 2n\pi)/2\pi f$ (for those traces with progressively more positive slopes) or $(\varphi_{\text{net}} - 2n\pi)/2\pi f$ (for those traces with progressively more negative slopes). To fit the model to the measured delays, the data in Fig. 6 were first sorted to create an 1800×8 matrix in which each row corresponds to a frequency at which data were collected, the first column contains $1/f$, and columns 2 through 8 contain seven data sets with delays of the form $\tau_m = \tau_s + (\varphi_{\text{net}} + 2n\pi)/2\pi f$ for integer $-3 \leq n \leq 3$, as depicted in Fig. 7.

The usual 1-D scalar transmission line model (Fig. 2) was used to model the acoustic coupling layer [4], [10]. When comparing the buffer rod reflection with the first sample reflection (labeled B and C in Fig. 1), the measured time delay, τ_m , is given by

$$\tau_m = \frac{2l_3}{v_3} + \frac{2\varphi_{T13} - \varphi_{R13} - \pi + 2\pi n}{2\pi f}, \quad (2)$$

where l_3 and v_3 are the path length and phase velocity of an acoustic wave in the sample, respectively. φ_{T13} and φ_{R13} are the phase shifts acquired by waves transmitted into the sample from the buffer rod and waves reflected back into the buffer rod from the buffer rod–couplant boundary, respectively. The acoustic wave undergoes a phase shift of $-\pi$ upon reflection from the sample–air boundary. Lastly, n is a positive or negative integer related to the cycles of the tone bursts that are being overlapped and is zero for the correct overlap. The transmission and reflection coefficients for normally incident stress plane waves in the three-media transmission line (see Fig. 2) have previ-

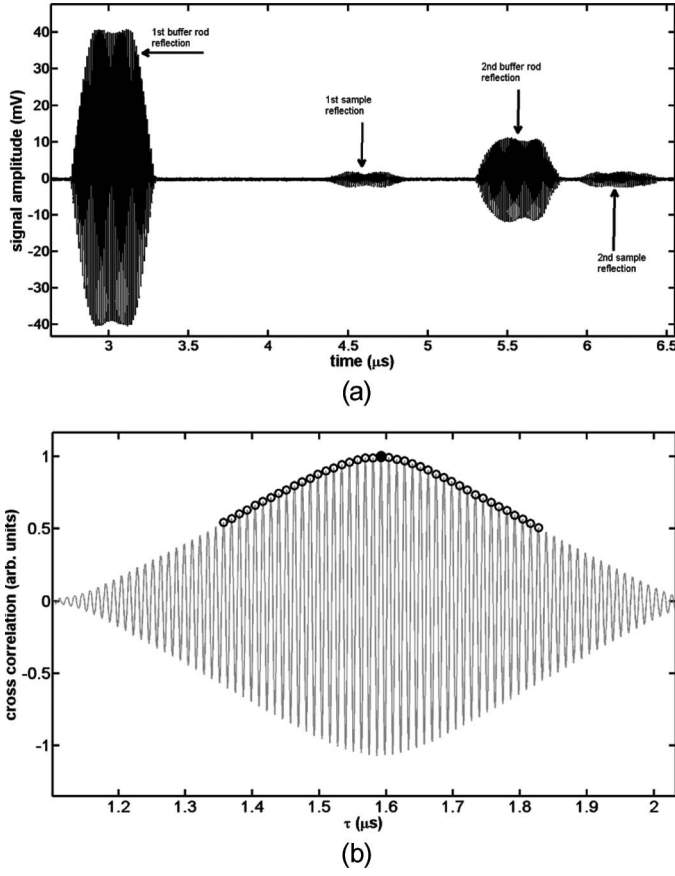


Fig. 5. (a) Two consecutive buffer rod and sample reflections as recorded on the oscilloscope for a typical delay measurement and (b) the cross-correlation function of the first buffer rod and first sample reflections. These reflections are windowed before carrying out the cross-correlation to avoid interference from echoes spaced similarly in time.

ously been derived [10], [11] but are reproduced here for convenience. The reflection, R_{xy} , and transmission coefficients, T_{xy} , are:

$$\begin{aligned} R_{13}^s &= \frac{(R_{12}^s - R_{32}^s e^{2ik_2 l_c})}{Y^s}, & R_{31}^s &= \frac{(R_{32}^s - R_{12}^s e^{2ik_2 l_c})}{Y^s}, \\ T_{13}^s &= \frac{(T_{12}^s T_{23}^s e^{ik_2 l_c})}{Y^s}, & T_{13}^s &= \frac{(T_{32}^s T_{21}^s e^{ik_2 l_c})}{Y^s}, \end{aligned} \quad (3)$$

where $Y^s = 1 - R_{12}^s R_{32}^s e^{2ik_2 l_c}$. $k_2 = 2\pi/\lambda_2$ is the wave number of the stress wave in the couplant and l_c is the thickness of the couplant. The subscript x represents the medium the wave is coming from (either 1 or 3 in Fig. 2) and the subscript y represents the medium the wave is traveling toward (either 1 or 3 in Fig. 2). The R_{ij} and T_{ij} on the right-hand sides of the relations in (3) (where i and j are consecutive numbers) are the familiar reflection and transmission coefficients for the two-media reflection or transmission case:

$$R_{ij}^s = \frac{Z_j - Z_i}{Z_j + Z_i}, \quad T_{ij}^s = \frac{2Z_j}{Z_j + Z_i}. \quad (4)$$

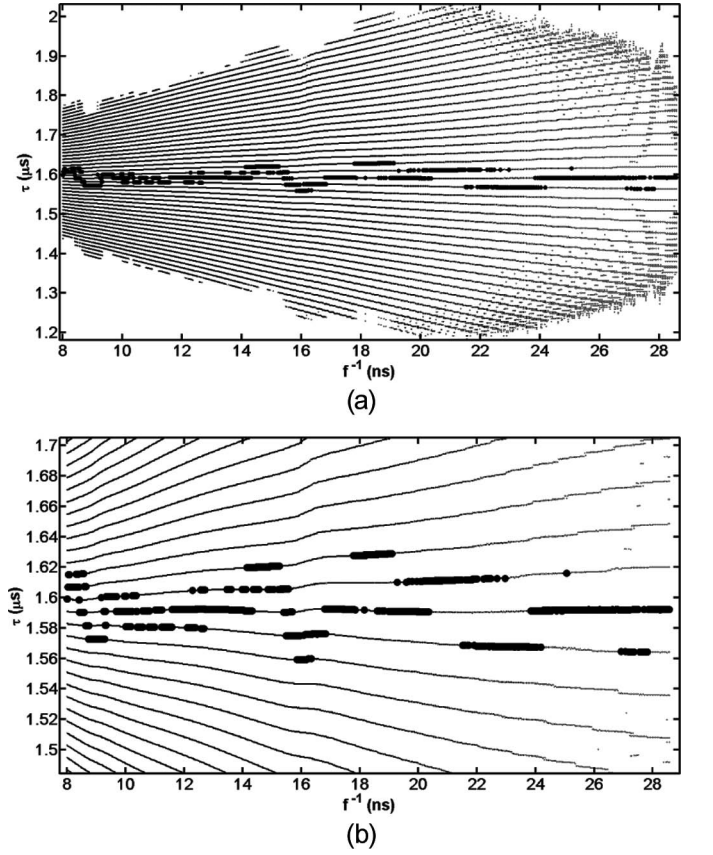


Fig. 6. (a) All delay data recorded between 35 and 125 MHz. The heavy black dots indicate the lag corresponding to the maximum in the cross-correlation function of the first buffer rod and sample reflections at each carrier frequency. The smaller gray dots represent the local maxima on either side of the global maximum in the cross-correlation function at each frequency. The scatter in the data at lower frequencies and far away from the maximum in the cross-correlation function reflect the weakness in the signal and the unreliability of the correlation function under those conditions. (b) The same data presented in (a), but focusing on the overlaps close in time to the correct overlap.

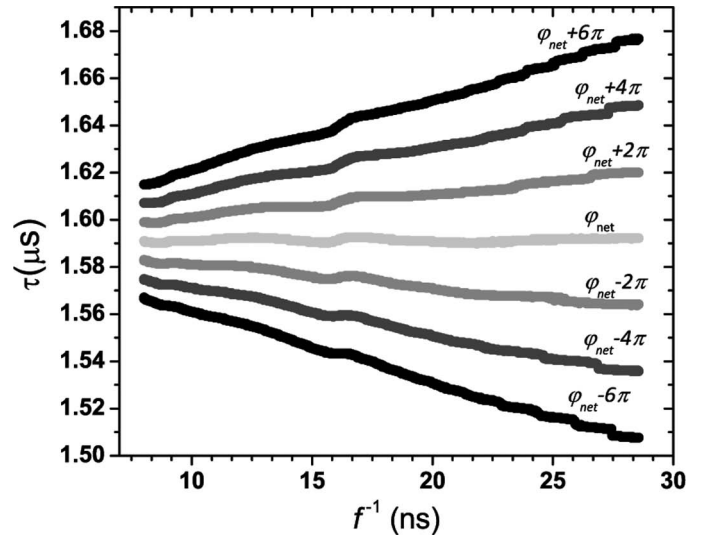


Fig. 7. Delay data after the data have been sorted into seven data sets. The f^{-1} dependence of each data set is indicated with the shallowest data set, with slope φ_{net} , corresponding to the correct overlap.

In (4), $Z_i = v_i \rho_i$ is the acoustic impedance of the i th medium. The superscript s throughout these relations serves as a reminder that these expressions are for stress, as opposed to displacement, waves.

It is important to note that, for the three-media case, the phase of the reflection and transmission coefficients depends on the frequency of the stress wave and the couplant thickness because of the presence of the $e^{ik_z l_c}$ and $e^{2ik_z l_c}$ terms. This is in contrast to the two-media case in which the phase is independent of frequency, as can be seen from (4).

Built into (1)–(4) is the assumption that the various media in the transmission line are nondispersive, and the v_i and Z_i are thus independent of frequency. When probing dispersive samples or making use of dispersive buffer rods or couplants, the frequency dependence of the v_i and Z_i should be included in the relevant terms of (1)–(4).

An implementation of the Nelder–Mead simplex direct search algorithm [13] was used to fit (2) to each sorted data set. Two other commonly used algorithms, the Levenberg–Marquardt method and a generalized reduced gradient (GRG2) algorithm, were also initially tested and both showed initial guess sensitivities similar to that of the Nelder–Mead simplex method. The nonlinear model has two free parameters, l_c and v_p , for which one must provide initial starting guesses to input into optimization routine. NLLS minimization routines locate local minima (instead of a global minimum), which are known to be sensitive to the initial guesses of the user [13]. For each of the seven data sets ($-3 \leq n \leq 3$), the norm of the difference vector, Δ , was calculated as

$$|\Delta| = \sqrt{\sum_i (\tau_{\text{meas}}(f_i) - \tau_{\text{fit}}(f_i))^2}, \quad (5)$$

where τ_{meas} is the measured delay and τ_{fit} is calculated at each point for which there is a measured delay using (2) and the appropriate phases of the reflection and transmission coefficients in (3). The summation is carried out for all frequencies at which there is a measured delay. To investigate how sensitive the minimization routine is to small changes in the parameters v_p and l_c , Δ for different NLLS solutions were calculated for initial guesses of couplant thicknesses between 10 and 50 μm (inclusive) in 2 μm intervals and for sample phase velocities between 6000 and 7000 m/s (inclusive) in 10 m/s intervals for a total of 2121 trials.

For comparison with the NLLS approach, linear least squares fits were also performed on the sorted data sets. This approach, which is computationally simpler, assumes that φ_{net} in (1) is a constant and independent of frequency.

IV. RESULTS AND DISCUSSION

A. RUS Sample Characterization

The alloy and associated acoustic material constants of the polycrystalline aluminum sample used in this work

were unknown because it was cut from machine shop stock. RUS was used to establish a reliable longitudinal acoustic phase velocity against which to compare the phase velocity determined by the couplant-corrected pulse–echo measurements. Twenty experimental resonances were fit using the LANL RUS code [16]. Fits were achieved by refining the values of C_{11} and C_{44} as well as the radius and height of the cylindrical sample. Varying the physical dimensions serves to refine the density because the measured mass was kept fixed. The refinement gave an RMS error of 0.19% and yielded a longitudinal phase velocity of 6360 m/s from a fit density of 2781 kg/m³ and a fit value of $C_{11} = 112.5$ GPa.

B. Delay Data Collected Between 35 and 50 MHz

Data collected within a 15 MHz frequency window were selected for an initial analysis because this spread represents a frequency range such as is typically used in PE measurements and also because the delay versus f^{-1} trends in this range are largely linear and do not exhibit the prominent phase change present around $f^{-1} = 16$ ns observed in Fig. 7. Fig. 8 shows the norm of the difference vector calculated after NLLS optimization using different starting values as described in Section III for the delay data collected in the frequency range $35 \text{ MHz} \leq f \leq 50 \text{ MHz}$ (delays in the range $20 \text{ ns} \leq f^{-1} \leq 29 \text{ ns}$ in Fig. 7). From Fig. 8, the high sensitivity of the norm of the difference vector to the initial guesses can be seen.

Each of the three vertical axes in Figs. 8(a)–8(c) show $|\Delta|$, whereas the horizontal axes show values of l_c and v_p corresponding to the solution (not the initial guesses) for the various initial guesses of these parameters. The different initial guess values, described in Section III, are not visible in the figures. Fig. 8(a) shows $|\Delta|$ as a function of both v_p and l_c , whereas Figs. 8(b) and 8(c) show the same $|\Delta|$ as a function of only v_p or l_c , respectively (in each, information about the second variable is not visible even though that variable changes from point to point). It can be concluded from Fig. 8 that the confident selection of either v_p , or l_c is not possible by searching for a minimum in $|\Delta|$. As seen in Fig. 8, the fit with the lowest $|\Delta|$ corresponds to $v_p = 6457$ m/s and $l_c = 50 \mu\text{m}$. When these parameters are entered into the model and plotted on top of the data (not shown), there are phase changes present in the model which are clearly not exhibited in the data. Based on performing a NLLS minimization with many different starting guesses, one is thus faced with a choice of selecting among multiple solutions for v_p in the range $6350 \text{ m/s} \leq v_p \leq 6460 \text{ m/s}$ with no quantitative basis for making such a selection.

Simple linear least squares fits were also performed on the seven data sets. As can be seen from (2), the intercept of such a fit determines the travel time in the sample whereas the slope is related to the net phase difference ($\pm 2n\pi$) between the two echoes being considered. A linear least squares fit to the delay data in the 35 to 50 MHz range gives a mean y -intercept value of 1.585 μs with an

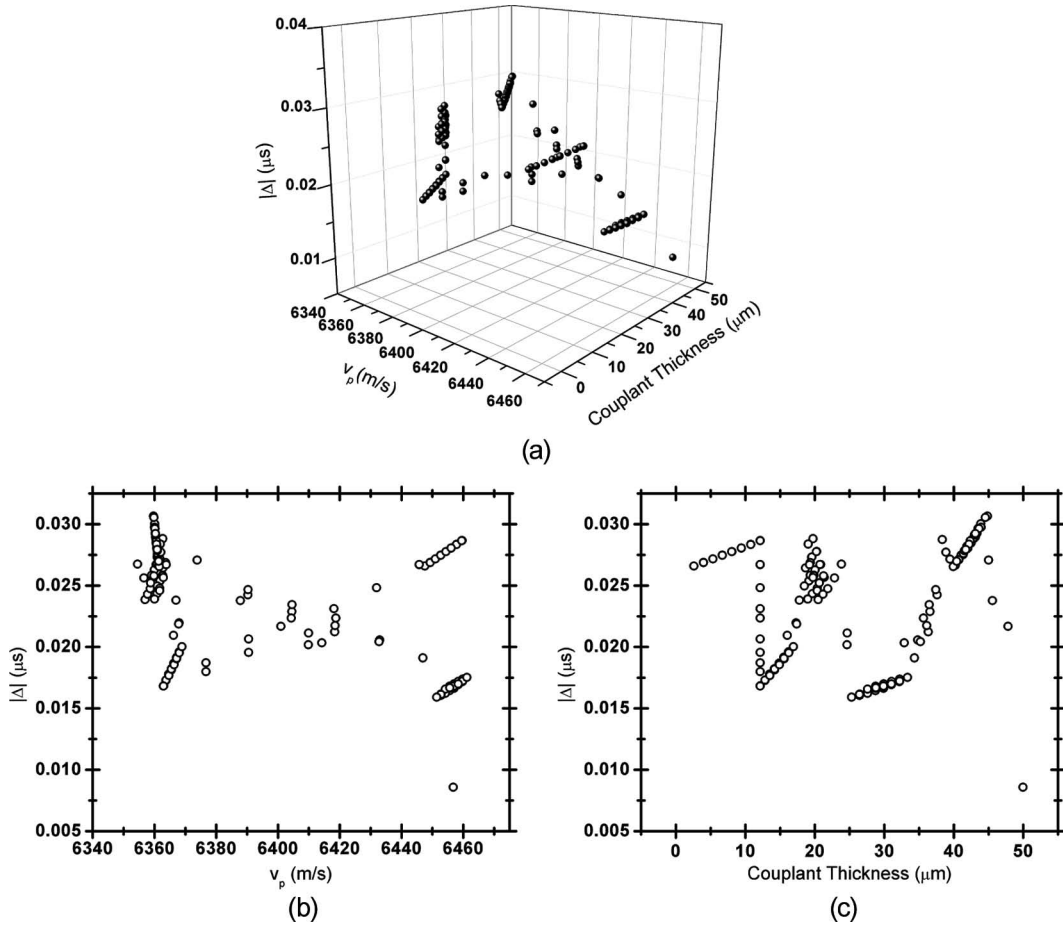


Fig. 8. The norm of the difference vector, $|\Delta|$, considering delays collected at carrier frequencies in the range $35 \text{ MHz} \leq f \leq 50 \text{ MHz}$. (a) The data represented as a function of both phase velocity, v_p , and couplant thickness, l_c . (b) and (c) show the same data as a function of a single variable only. (Note that the value of the second variable is changing from point to point in (b) and (c) even though this information is not visible.)

uncertainty of 0.2 ns when all seven data sets are considered. The uncertainty in the delay determination was estimated by using the standard error of the y -intercepts of the seven linear fits to the data. This delay yields a phase velocity of 6384.9 m/s for the 5.06 mm sample. This result agrees with the RUS-determined velocity to better than 0.4% which is good by most standards and certainly better than the 1.6% discrepancy one would get by choosing the $v_p = 6460$ m/s solution from the NLLS fit [see Fig. 8(b)]. Table I summarizes the different phase velocities and couplant thicknesses determined from this PE data set for easy comparison.

C. Delay Data Collected Between 35 and 125 MHz

Fig. 9 shows the results of the NLLS optimization trials with the same combinations of initial guesses as in Fig. 8 but considers delays collected at frequencies over the full range of $35 \text{ MHz} \leq f \leq 125 \text{ MHz}$. The layout of Fig. 9 is the same as that of Fig. 8: Fig. 9(a) shows $|\Delta|$ as a function of both v_p and l_c , whereas Figs. 9(b) and 9(c) show $|\Delta|$ as a function of these two parameters independently. As with the delay data from the 35 to 50 MHz range, the sensitivity of the optimization routine to the user-input initial guesses is evident. For example, if one

TABLE I. SUMMARY OF PULSE-ECHO-DETERMINED v_p AND l_c .

Data set	Least squares fit type	v_p (m/s)	δ_{RUS}^a (%)	l_c (μm)
PE 35–50 MHz	Nonlinear	6457	1.5	50
	Nonlinear	6350–6460	0.2–1.6	10–40
	Linear	6384.9	0.4	— ^b
PE 35–125 MHz	Nonlinear	6361	0.02	12–23
	Nonlinear	6361	0.02	40–42
	Linear	6360.9	0.01	— ^b

^a $\delta_{\text{RUS}} = 100 \cdot (v_p - v_{p,\text{RUS}}) / v_{p,\text{RUS}}$, where $v_{p,\text{RUS}} = 6360$ m/s.

^b l_c not determined in linear least squares fit.

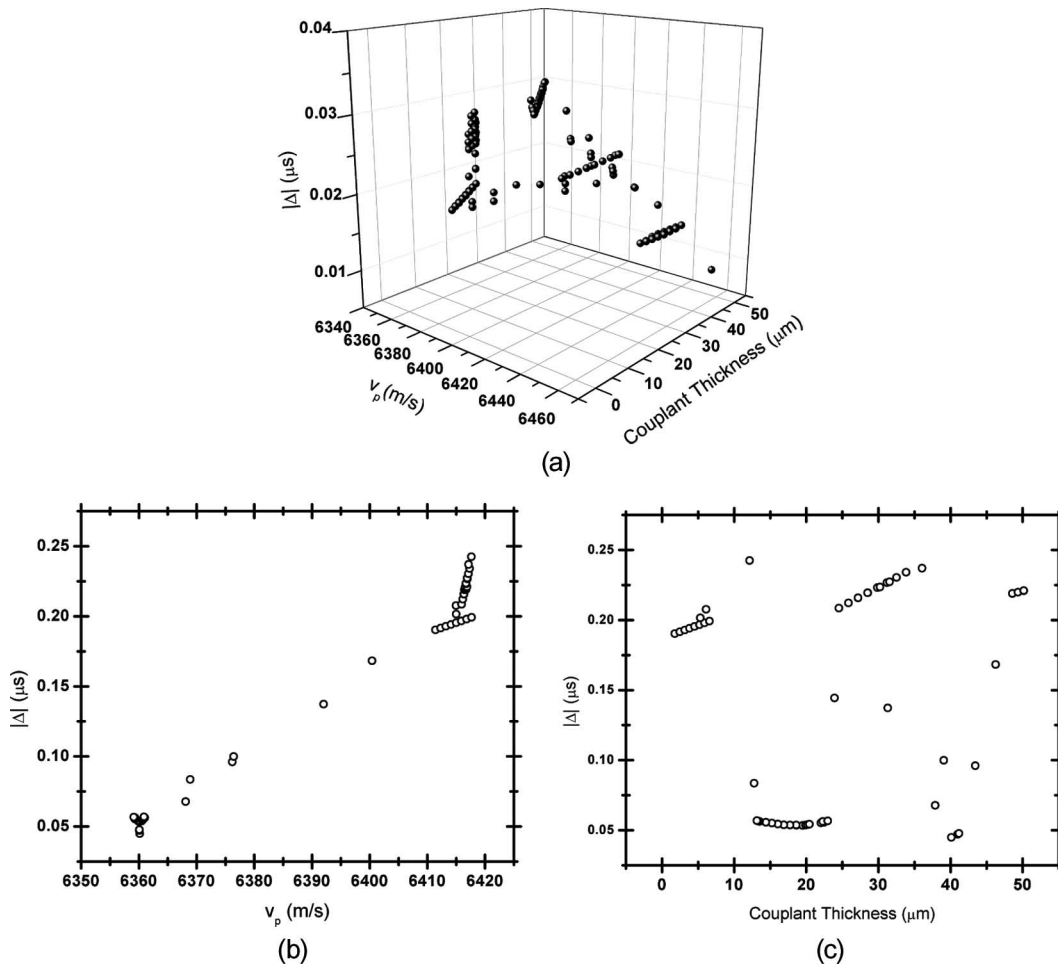


Fig. 9. The norm of the difference vector, $|\Delta|$, considering delays collected at all carrier frequencies in the range $35 \text{ MHz} \leq f \leq 125 \text{ MHz}$. (a) The data represented as a function of both phase velocity, v_p , and couplant thickness, l_c . (b) and (c) show the same data as a function of a single variable only. (Note that the value of the second variable is changing from point to point in (b) and (c) even though this information is not visible.)

were to run the optimization routine on the data in Fig. 7 a single time with starting guesses of $l_c = 30 \mu\text{m}$ and $v_p = 6400 \text{ m/s}$, the search terminates with a solution of $l_c = 24.5 \mu\text{m}$ and $v_p = 6416 \text{ m/s}$, which is seen to be far away from the global minimum in Fig. 9. The scatter of the possible solutions in Fig. 9 shows clearly that distinguishing the global minimum from the large number of local minima requires executing the optimization routine with many different starting values. Physical knowledge of a system often provides a useful basis for rejecting local minima in nonlinear minimizations. However, as can be seen from Figs. 8 and 9, in the case of the PE transmission line model, this would require prior knowledge of the couplant thickness to better than a few micrometers. This is not practical in most laboratory setups. It is also possible to change the maximum allowable $|\Delta|$ that the NLLS routine will accept before terminating (and thus reducing the number of solutions attainable). However, there is no way of knowing what this threshold $|\Delta|$ should be *a priori* because some data sets will naturally be fit more easily than others. Consequently, it will always be necessary to try many possible initial guesses when using an NLLS fitting routine to model PE delay data.

There is a group of solutions near $v_p = 6360 \text{ m/s}$ in Figs. 9(a) and 9(b) that have markedly lower $|\Delta|$ than the other solutions shown in the figure. However, within this group are solutions corresponding to two different bond length values, specifically $l_c \approx 12$ to $23 \mu\text{m}$ and $l_c \approx 40$ to $42 \mu\text{m}$, as can be seen in Figs. 9(a) and 9(c). Fits of (2) to the data are shown in Figs. 10(a) and 10(b) for values of $l_c = 13.5 \mu\text{m}$ and $l_c = 40 \mu\text{m}$, respectively (both fits had $v_p = 6361 \text{ m/s}$). The $|\Delta|$ of these two fits are too close to quantitatively reject one fit in favor of another. Note that both fits qualitatively capture the phase change in the delay data that is present around $f^{-1} = 16 \text{ ns}$ ($f = 62.5 \text{ MHz}$). Figs. 10(c) and 10(d) show close ups of the correct-overlap data [i.e., $n = 0$ in (2)]. The model of the system with a $40 \mu\text{m}$ bond length [Figs. 10(b) and 10(d)] appears to capture a feature in the data present around $f^{-1} = 12.5 \text{ ns}$ which is not captured in the $l_c = 13.5 \mu\text{m}$ model. However, the $l_c = 40 \mu\text{m}$ model also predicts features around $f^{-1} = 9 \text{ ns}$ and $f^{-1} = 24 \text{ ns}$ which are not seen in the data. Thus, though the v_p of the wave appears to be very precisely determined by the NLLS minimization, it is difficult to determine the bond length with the same certainty.

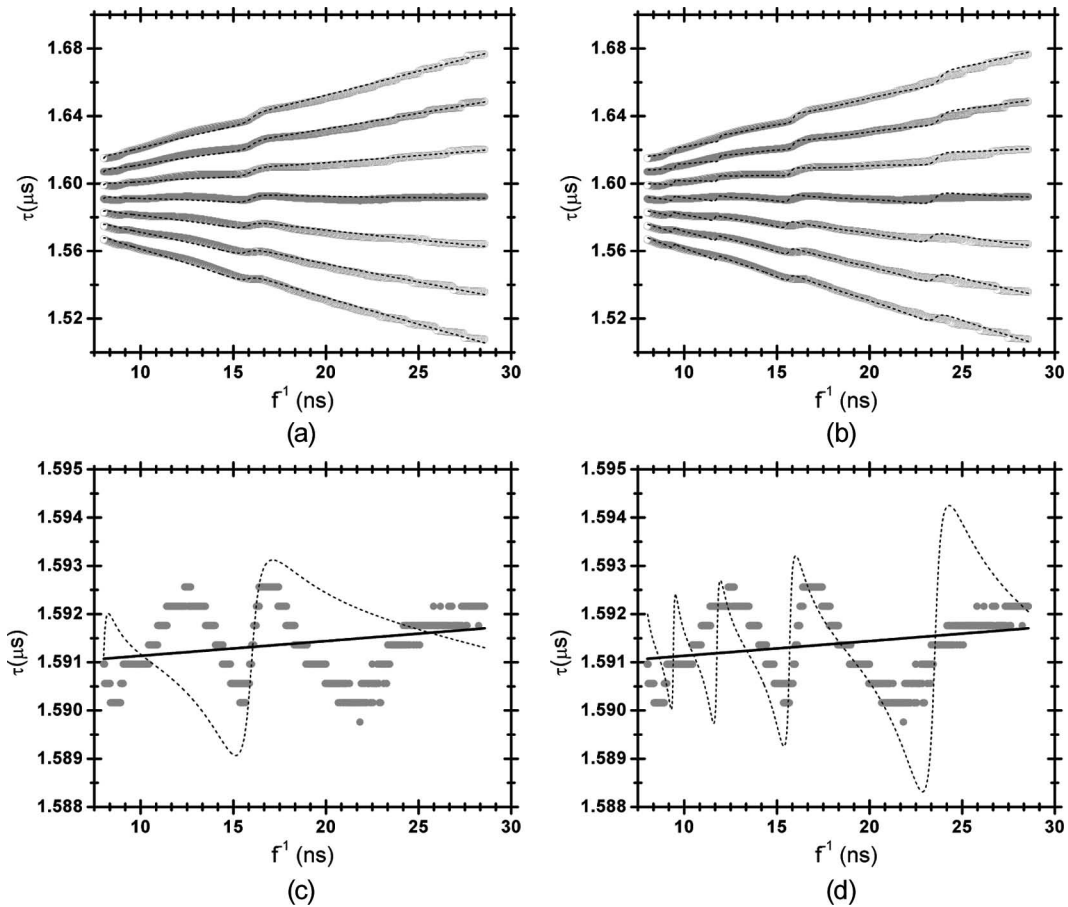


Fig. 10. The model fit data (black dashed line) is shown on top of the measured delay data (gray data points) for a phase velocity of 6361 m/s and couplant thicknesses of (a) and (c) 13.5 μm and (b) and (d) 40 μm . (c) and (d) show the detail of the trace with a slope of φ_{net} ($n = 0$) in panels (a) and (b), respectively.

A linear least squares fit to the full delay data set, shown in Figs. 10(c) and 10(d), gives a delay of $1.591 \mu\text{s} \pm 0.1 \text{ ns}$ when all seven data sets were considered. The relative error in the delay determination is thus on the order of 10^{-4} . This delay corresponds to a $v_p = 6360.9 \text{ m/s}$, which is in excellent agreement with the velocities determined using the NLS minimization and also with the RUS results. Further, the $|\Delta|$ of 30 ns calculated from the linear least squares fit indicates slightly better agreement with the data than the lowest $|\Delta| \approx 50 \text{ ns}$ calculated from the NLS fit. The velocities and bond lengths determined from this data set are compared with those determined from the 35 to 50 MHz data set in Table I.

D. The Number of Points Required for Delay Determination

This analysis emphasizes the importance of measuring acoustic phase delays at multiple frequencies for PE v_p determinations. Cross-correlation of digital signals is a powerful tool that is useful for removing biases that can occur when overlapping the echoes by eye. However, even using the maximum of the cross-correlation function, it is easy to choose the wrong overlap by several full cycles, as can be seen in Fig. 6. For example, if a single delay measure-

ment were made at 52.6 MHz ($f^{-1} = 19 \text{ ns}$) or 62.5 MHz ($f^{-1} = 16 \text{ ns}$) and the cross-correlation maximum were chosen as the final delay, the delay would differ from the true delay at that frequency by +2 or -2 whole periods, respectively. At 52.6 MHz and 62.5 MHz, these errors are 38 ns and -32 ns, respectively, corresponding to a +2.4% and -2.0% deviation from the true delay and errors of 4.8% and 4.0% in elastic constants extracted from these measurements.

Given the commercial availability of broadband transducers and the ease of automated data collection and digital signal processing, it is straightforward to collect data at many different frequencies. The limiting factors in the number of data points collected need only be the center frequency and bandwidth of the transducer, the physical size and acoustic attenuation coefficients of the material used, and the time available for data collection. In practical measurements, one would like to collect enough data points to achieve the precision required by his application and no more. One way to accomplish this would be first to collect delay data at the maximum, minimum and middle frequencies of the available bandwidth. A linear least squares fit to these data can be performed and the y -intercept recorded. Next, data would be collected at frequencies halfway between each of the first three frequen-

cies, giving a total of five data points. The y -intercept of the fit to five data points can be compared with the intercept of the fit using only three points to determine if the fit parameters are changing by the inclusion of additional data. The process of successively increasing the number of data points and watching for a change in the fit delay time would be repeated until the determined delay stabilizes to within the precision required by the application. The full data set reported in this work was analyzed as if the data were collected in the manner described here and it was determined that 129 data points were sufficient for analyzing these data. Fits performed using 257, 513, and 1025 equally spaced data points found delays that were all within ten parts per million of the iteration immediately before and also were all within five parts per million of the fit to all 1800 data points.

V. CONCLUSIONS

This paper presents acoustic pulse–echo data with delays collected over a very large range of tone-burst carrier frequencies to explicitly demonstrate the strong nonlinearities in the delay data predicted by the commonly used transmission line model. The data analysis presented in this work has compared the effectiveness of the three-media scalar transmission line model that is commonly used in accounting for the coupling layer in pulse–echo time-of-flight measurements to the much more simple linear least squares fit to the data. Corrections made with the transmission line model require the use of a two-parameter nonlinear least squares minimization routine which can easily lead to significant differences in extracted acoustic phase velocities and coupling bond lengths depending on the user-input initial guesses of these parameters. Measurements of acoustic delays using pulses with carrier frequencies ranging from 35 to 125 MHz showed that the nonlinear least squares fitting routine can identify a phase velocity value in good agreement with that determined through RUS measurements if enough trial guesses are used. However, the model was unable to provide a quantitative criterion for unambiguously determining the coupling bond length. Moreover, the phase velocity determined by the NLLS fit showed negligible difference to that found using the more simple linear least squares fit. When delays collected from a more modest carrier frequency range of 35 to 50 MHz were considered, the NLLS routine was unable to unambiguously identify either the phase velocity or bond length. A simple linear least squares fit of these same data indicated a phase velocity within half of a percent of that determined using RUS and the broader frequency range pulse echo measurements. The strongest argument in favor of the transmission line model over a simple linear least squares fit to delay data may be that, in theory, it provides information about the couplant bond length but this argument is not supported by the data reported here. This work suggests that a simple linear least squares fit to phase delay versus inverse frequency should be used in fa-

vor of the complex nonlinear least squares fit which results from the transmission line model. This is particularly true given that the latter does not provide unambiguous values for the bond length and can often lead to inaccurate values for the phase velocity.

REFERENCES

- [1] H. B. Huntington, "Ultrasonic measurements on single crystals," *Phys. Rev.*, vol. 72, no. 4, pp. 321–331, 1947.
- [2] R. Truell, C. Elbaum, and B. Chick, "Measurement of attenuation and velocity by pulse methods," in *Ultrasonic Methods in Solid State Physics*. New York, NY: Academic, 1969.
- [3] ANSI/IEEE Standard on Piezoelectricity, standard 176-1987, 1987.
- [4] B. T. Sturtevant, P. A. Davulis, and M. Pereira da Cunha, "Pulse echo and combined resonance techniques: A full set of LGT acoustic wave constants and temperature coefficients," *IEEE Trans. Ultrason. Ferroelectr. Freq. Control*, vol. 56, pp. 788–797, Apr. 2009.
- [5] W. D. Wilson, "Speed of sound in distilled water as a function of temperature and pressure," *J. Acoust. Soc. Am.*, vol. 31, no. 8, pp. 1067–1072, 1959.
- [6] W. D. Wilson, "Speed of sound in sea water as a function of temperature, pressure, and salinity," *J. Acoust. Soc. Am.*, vol. 32, no. 6, pp. 641–644, 1960.
- [7] D. K. Mak, "Couplant correction for ultrasonic velocity-measurements," *Br. J. Nondestruct. Test.*, vol. 33, pp. 344–346, Jul. 1991.
- [8] D. K. Mak, "Ultrasonic phase-velocity measurement incorporating couplant correction," *Br. J. Nondestruct. Test.*, vol. 35, pp. 443–449, Aug. 1993.
- [9] H. J. Mcskimin, "Pulse superposition method for measuring ultrasonic wave velocities in solids," *J. Acoust. Soc. Am.*, vol. 33, no. 1, pp. 12–16, 1961.
- [10] C. Pantea, D. G. Rickel, A. Migliori, R. G. Leisure, J. Z. Zhang, Y. S. Zhao, S. El-Khatib, and B. S. Li, "Digital ultrasonic pulse–echo overlap system and algorithm for unambiguous determination of pulse transit time," *Rev. Sci. Instrum.*, vol. 76, no. 11, art. no. 114902, Nov. 2005.
- [11] H. A. Spetzler, G. Chen, S. Whitehead, and I. C. Getting, "A new ultrasonic interferometer for the determination of equation of state parameters of submillimeter single-crystals," *Pure Appl. Geophys.*, vol. 141, no. 2–4, pp. 341–377, 1993.
- [12] A. W. Nolle and S. C. Mowry, "Measurement of ultrasonic bulk-wave propagation in high polymers," *J. Acoust. Soc. Am.*, vol. 20, no. 4, pp. 432–439, 1948.
- [13] J. A. Nelder and R. Mead, "A simplex-method for function minimization," *Comput. J.*, vol. 7, no. 4, pp. 308–313, 1965.
- [14] F. J. Harris, "Use of windows for harmonic-analysis with discrete Fourier-transform," *Proc. IEEE*, vol. 66, no. 1, pp. 51–83, 1978.
- [15] D. N. Sinha and G. Kaduchak, "Noninvasive determination of sound speed and attenuation in liquids," in *Experimental Methods in the Physical Sciences*, vol. 39, M. Levy, H. E. Bass, and R. Stern, Eds., New York, NY: Academic Press, 2001, pp. 307–333.
- [16] A. Migliori and J. L. Sarrao, *Resonant Ultrasound Spectroscopy*. New York, NY: Wiley, 1997.
- [17] W. H. Press, S. A. Teukolsky, W. T. Vetterling, and B. P. Flannery, *Numerical Recipes in C*, 2nd ed., New York, NY: Cambridge University Press, 1992.



Blake Sturtevant (S'06–M'10) was born in Waterville, ME, in 1981. He received an A.B. degree in physics from Bowdoin College, Brunswick, ME, in 2003. He earned a Ph.D. degree in physics from the University of Maine, Orono, ME, in 2009 with a thesis titled "Ultrasonic characterization of single crystal langatate."

Since 2010, Dr. Sturtevant has been a Postdoctoral Research Associate at Los Alamos National Laboratory in Los Alamos, NM. His research has focused on the acoustic characterization of materials, particularly liquids, at high temperature and pressure.

Dr. Sturtevant is a member of the IEEE and the American Physical Society (APS). He is a reviewer for the *IEEE Transactions on Ultrasonics, Ferroelectrics, and Frequency Control*.



Cristian Pantea was born in Romania in 1972. He received a B.Sc. degree in physics from University of Cluj, Cluj-Napoca, Romania, in 2005, and a M.Sc. degree in physics, in 2006, from the same university. He earned a Ph.D. degree in physics from Texas Christian University, Fort Worth, TX, in 2004 with a thesis titled “Kinetics of diamond-silicon reaction under high pressure-high temperature conditions.”

Between 1996 and 2000, he worked as a Graduate Research Assistant at the Institute of Chemistry in Cluj-Napoca, Romania. From 2003 to 2004, he worked as a Graduate Research Assistant at Los Alamos National Laboratory, and from 2004 to 2007 as a Postdoctoral Research Associate at the same institution. Since 2007, Dr. Pantea has been a Research Scientist at Los Alamos National Laboratory. His research has focused on different acoustic techniques for materials characterization (pulse-echo, resonant ultrasound spectroscopy, swept-frequency acoustic interferometry, acoustic nonlinearity) and development of acoustic sensors and methods for materials characterization.

Dr. Pantea is a member of the Acoustical Society of America (ASA) and the Neutron Scattering Society of America (NSSA). He is a reviewer for several journals, including *Phys. Rev. Lett.* and *Phys. Rev. B*.



Dipen Sinha was born in India in 1951. He received his B.Sc. degree with Physics Honors from St. Xavier's College, Ranchi, India, in 1970. He obtained an M.Sc. degree in physics and a Diploma in industrial physics from the Indian Institute of Technology, Kharagpur, India, in 1972 and 1973, respectively. He received his Ph.D. degree in physics from Portland State University, OR, in 1980. He joined the Los Alamos National Laboratory (LANL) as a postdoctoral fellow in 1980. He moved to California to work with the Rockwell

International Corporation as a staff scientist in 1983. He returned to the Los Alamos National Laboratory as a scientist in 1986 and is currently a laboratory fellow. He also leads the Acoustics and Sensors team at LANL. His research interests include the development of novel acoustics-based sensors and engineered materials. Dr. Sinha is a member of the American Physical Society and the Acoustical Society of America.